Appl. Phys. B 82, 275–281 (2006)
DOI: 10.1007/s00340-005-2033-9

Applied Physics B
Lasers and Optics

J. SCHWARZ[1,✉]
M. RAMSEY[2]
D. HEADLEY[3]
P. RAMBO[1]
I. SMITH[1]
J. PORTER[1]

Thermal lens compensation by convex deformation of a flat mirror with variable annular force

[1] Sandia National Laboratories, P.O. Box 5800 MS 1193, Albuquerque, NM 87185-1193, USA
[2] Comforce Technical Services, Sandia National Laboratories, P.O. Box 5800 MS 1193, Albuquerque, NM 87185-1193, USA
[3] American Staff Augmentation Providers, Sandia National Laboratories, P.O. Box 5800 MS 1193, Albuquerque, NM 87185-1193, USA

Received: 28 February 2005/
Revised version: 9 September 2005
Published online: 15 December 2005 • © Springer-Verlag 2005

ABSTRACT An optical surface with convex parabolic shape over a large area has been created using a 12.7-mm-diameter annular pusher to deform a flat 25.4-mm-diameter mirror. The deformable mirror assembly has been modeled using finite element analysis software as well as analytical solutions. The measured parabolic surface deformation shows good agreement with those models. Mirror performance was studied using a Shack–Hartman wavefront sensor and the mirror has been applied to compensate thermal lensing in a Nd:YAG rod amplifier.

PACS 41.85.Ct; 42.60.Da

1 Introduction

Thermal lensing plays an important role in solid state laser amplification. Due to the limited conversion efficiency of pump power to laser light, a considerable thermal load is deposited in the amplifier material. Radial pump symmetry causes a parabolic temperature profile in the laser rod and leads to thermal lensing. The resulting radial change of index of refraction $\Delta n(r)$ as a function of radius r inside the laser rod is [1]

$$\Delta n(r) = -\frac{Q}{4K}\frac{\mathrm{d}n}{\mathrm{d}T}r^2 , \qquad (1)$$

where Q is the heat generated per unit volume, K is the thermal conductivity, and $\mathrm{d}n/\mathrm{d}T$ is the change of refractive index n with temperature T. The parabolic variation of the refractive-index change leads to a thermal lensing effect and introduces a positive lens into the optical system. A common method for compensating this effect is to introduce a negative lens of equal focal length. However, since these focal lengths are typically on the order of meters, they are difficult to measure precisely and appropriate compensating lenses are rarely available. Therefore, adjustable focal length elements are introduced, by using an intracavity telescope [2], a self-compensating negative lens [3, 4], or a deformable cavity mirror [5, 6]. In some cases [6], mirrors are deformed by applying a point-like force at the center of the rear surface. This leads to a strong localized deformation at the center and a curvature profile which is neither spherical nor parabolic. We have improved upon the latter deformable mirror approach to allow good parabolic deformation for efficient thermal lens compensation.

2 Mirror design

Our design uses an annulus to push on the back surface of a flat mirror substrate, simply supported at the outer edge, to create a parabolic deformation within the encircled area of that annulus. Figure 1 shows the calculated difference between a center push and an annular push for a 25.4-mm-diameter BK7 mirror with a thickness of 3.2 mm and a center deflection of 13.2 μm. Assuming flat, circular substrates with thicknesses less than 1/4 of the diameter and deflections less than 1/2 of the thickness, these surface deformations can be calculated using analytical solutions [7]. For a point force W pushing on a circular substrate of thickness t and substrate

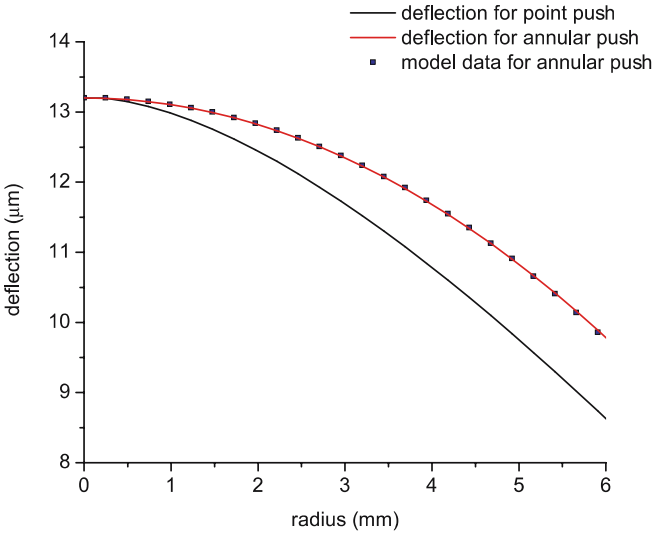

FIGURE 1 Plot of theoretical deflection versus radius for a 25.4-mm-diameter, 3.2-mm-thick BK7 substrate assuming a point-like center push from (2) (*black*) and an annular pusher of 6-mm radius in (3) (*red*). It can be seen that there is good agreement between the analytical solution (not a fit!) and the finite element analysis data (*blue squares*)

✉ Fax:+ 1 505-844-2159, E-mail: jschwar@sandia.gov

radius a, the deflected profile $y(r)$ is given by

$$y(r) = -\frac{W}{16\pi D}\left[\frac{3+\nu}{1+\nu}\left(a^2 - r^2\right) - 2r^2 \ln\frac{a}{r}\right], \quad (2)$$

where $D = Et^3/(12(1-\nu^2))$, $E = 82 \times 10^9$ Pa is the modulus of elasticity for BK7 [8], $\nu = 0.206$ is Poisson's ratio [8], and r (with $0 \le r \le a$) is the radius. Equation (2) reveals that the resulting surface deformation cannot be parabolic or even spherical. However, a ring pushing on a flat substrate with simple circular edge support will always lead to a parabolic surface deformation inside the ring diameter. This can clearly be seen in (3). For a given annular line force w, the deflected profile $y(r)$ inside the ring diameter r_0 is given by [7]

$$y(r) = y_c + \frac{M_c r^2}{2D(1+\nu)}, \quad \text{where}$$
$$y_c = -\frac{wa^3}{2D}\left(\frac{C_1}{1+\nu} - 2C_2\right) \quad (3)$$

is the center deflection, $M_c = waC_1$ is the moment at the center, and C_1 and C_2 are constants:

$$C_1 = \frac{r_0}{a}\left[\frac{1+\nu}{2}\ln\frac{a}{r_0} + \frac{1-\nu}{4}\left[1 - \left(\frac{r_0}{a}\right)^2\right]\right],$$

$$C_2 = \frac{r_0}{4a}\left[\left[\left(\frac{r_0}{a}\right)^2 + 1\right]\ln\frac{a}{r_0} + \left(\frac{r_0}{a}\right)^2 - 1\right]. \quad (4)$$

One should note that (3) and (4) are only valid for values $0.2 \le r_0/a \le 0.8$. Below this limit the situation should be modeled using a point load (see (2)). Once r_0/a exceeds 0.8, the ring radius r_0 approaches the radius a and these equations no longer apply [7].

The applicability of the analytical solutions to the actual three-dimensional geometry was verified by using a one-fourth finite-element model to analyze the behavior of a simply supported BK7 optic under a uniformly distributed annular force. The design of the holder assembly can be seen in Fig. 2. Detailed deflection and stress analysis (see Fig. 3) were performed using the finite-element software for various annular forces. Several contact scenarios were modeled, including slip, separation, and friction. All relevant parts were included in the analysis model. These considerations lead to a finite element analysis model that approximated the real apparatus with a far greater level of detail than the simple assumptions of analytical solutions. The finite element analysis results were compared to Roark's analytical solutions [7] and show good agreement (see Fig. 1). This agreement gave sufficient confidence to use the simpler analytical expressions in place of the more complicated finite element analysis model. Therefore, the analytical expressions have been used in the later discussion.

Design constraints motivated a streamlined and lightweight solution. Delrin 150, A2 tool steel, and 6061T6 aluminum were chosen for their material properties and machinability. The optic is simply supported near its edge in the bore of a Delrin 150 housing. No special alignment is performed. The piston, which is also made from Delrin 150, contains the annu-

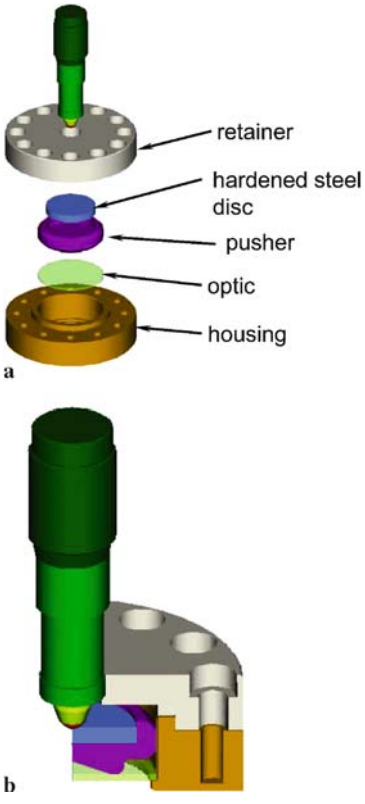

FIGURE 2 (**a**) Deformable mirror assembly and its components. (**b**) Detailed view of the contact area between the retainer and the optic

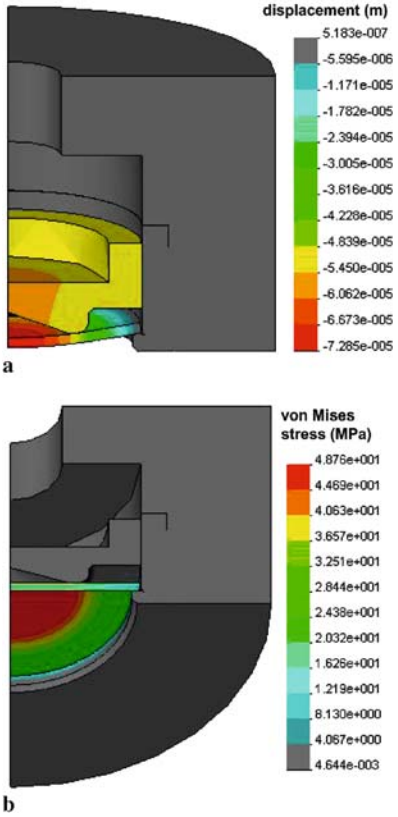

FIGURE 3 (**a**) Finite-element model for a 13.2-μm center deflection on a 1-mm-thick and 25.4-mm-diameter mirror. Note: the depicted deflection is exaggerated. (**b**) Stress plot for the corresponding deflection

lus whose diameter is smaller than the support rim. The radial gap tolerance between the piston outer diameter and the housing bore (see Fig. 2) ranges from 12.7 μm to 25.4 μm (0.0005″ to 0.001″). Hardened tool steel is used to transfer the point load from the micrometer to the piston. The retainer is made from aluminum in order to adequately support the force from the micrometer. Lastly, the assembly is designed to fit into a standard 2″ optic mount for ease of use.

Mechanical tolerances are important, as one might imagine. Radial symmetry makes this assembly easy to produce on a lathe, but material irregularities and machining errors are still a problem. Both the Delrin 150 and the aluminum parts were taken from rod stock to reduce non-radial internal stresses that would be present in an extruded plate. Concentricity is inherently good since most critical features are made in a single setup on a lathe. The flatness of the Delrin 150 pushing ring features on the piston and housing were held within a 25.4 μm (0.001″) window. That value was chosen for cost control and it proved to be sufficiently good for some applications, but could be improved. High-frequency deviations of flatness on the Delrin 150 parts may be flattened once a force is applied to the hard optic while low-frequency deviations may be preserved. It should be noted that standard machining processes cannot yield a surface tolerance much better than 12.7 μm (0.0005″). A computer-controlled grinder is necessary to achieve better tolerances.

This mechanical design concept can be used with larger substrates and larger-area convex mirrors are easily achievable for use in large-beam applications. For a 25.4-mm substrate the usable area can be expanded by increasing the ring diameter. In principle, this should not affect the performance of the mirror holder; however, it will increase the force required on the annular pusher. Figure 4 shows the force needed to achieve a focal length of −3.05 m for various pusher diameters and thicknesses on a 25.4-mm mirror. The shortest focal length is limited by the tensile stress of 51.7 MPa (7500 psi) that can be applied to the BK7 mirror substrate before fracture occurs. Figure 5 shows the shortest focal length obtainable (limited by the 51.7-MPa stress limit) versus mirror thickness for several pusher radii. One should note that the shortest possible focal length not only decreases with thickness but also with pusher radius, since stresses will be reduced in those cases. It can be seen from the previous discussion that for many applications there are an optimal mirror thickness and a pusher radius that should satisfy the optical requirements.

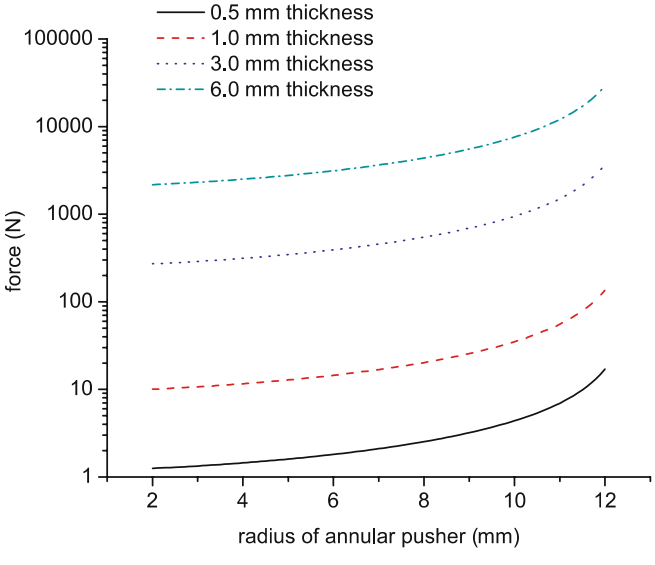

FIGURE 4 Plot of force versus annular pusher radius for a 25.4-mm-diameter mirror at various thicknesses and a fixed focal length of 3.05 m

3 Wavefront measurements

A Shack–Hartmann sensor was used to perform wavefront measurements on the deformable mirror assembly. A 100-mW, 1054-nm diode-pumped laser from Crystalaser was expanded to a 'clean' 7-cm-diameter beam by spatially filtering with a 5-μm pinhole between $f = 6$ mm and $f = 31$ cm lenses. To ensure a flat and uniform wavefront, the beam was apertured down to 10 mm before being reflected off the deformable mirror.

The wavefront was then analyzed using a Shack–Hartmann sensor from Adaptive Optics Associates. This sensor consists of a lenslet array (part no. 250-S-018) with a focal length of $f = 18$ mm and a lenslet separation of 250 μm over an area of 15 × 15 mm. The array is backed by a Pulnix TM-9701 CCD camera with a sensor area of 8.9 × 6.6 mm. An overview of the setup is depicted in Fig. 6.

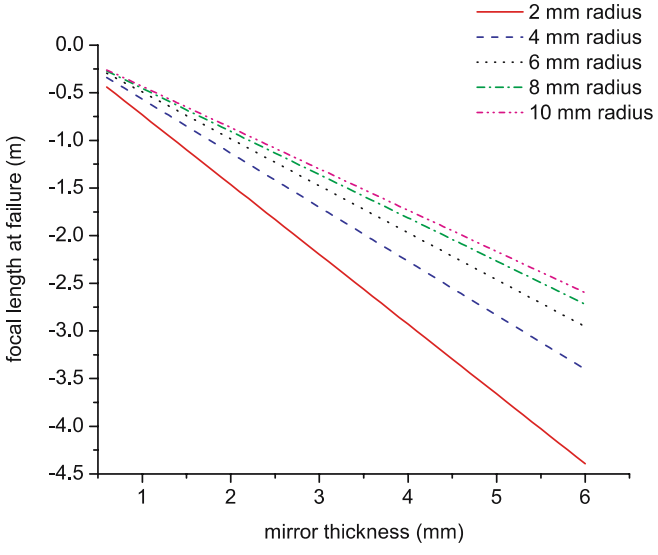

FIGURE 5 Plot of failure-limited focal length versus mirror thickness for a 25.4-mm mirror and several pusher radii

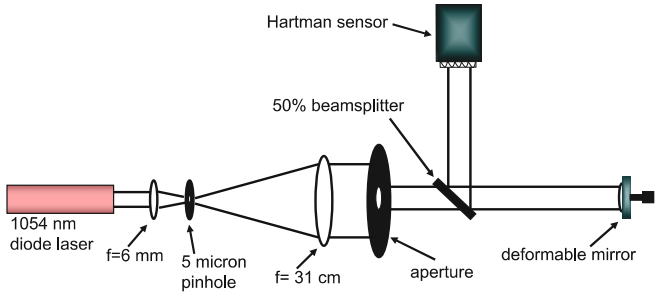

FIGURE 6 Setup for wavefront measurement

Measurements were performed on two substrates: (a) a 25.4-mm-diameter, 3.2-mm-thick BK7 substrate with a 1054-nm coating at 0°, (b) a 25.4-mm-diameter, 1-mm-thick BK7 substrate with a 1054-nm coating at 0°. The setup and software were calibrated using a commercial flat 2″ diameter, $\frac{1}{2}''$ thick mirror as a reference. This baseline measurement was used to determine the offset from a flat mirror surface. The mirror was then slightly deformed by slowly turning the micrometer at the back of the mirror holder and the wavefront data was stored in a two-dimensional array.

Using Matlab, the data was then plotted and fitted to a sphere in order to determine the radius R of the wavefront (see Fig. 8a). The data is fitted to a sphere because the reflection of a plane wavefront from a parabolic surface results in a spherical wavefront. After measuring the distance d of the wavefront sensor from the deformable mirror, the focal length f of that convex mirror can easily be approximated by $f = R - d$. Tables 1 and 2 show detailed measurements of the measured focal lengths for 1-mm and 3.2-mm-thick mirrors. It can be seen that focal lengths of tens of meters down to the sub-meter scale can be accommodated. The error in focal length was calculated by taking the RMS deviation of 40 circular fits to equally spaced radial lineouts around the sphere. The larger errors in spherical fitting for long focal length are due to the fact that the center deformation of the mirror approaches the resolution of the Hartmann sensor. Hence, noise in the sensor has a large effect on the fitted sphere and on the resulting calculated focal length. In addition, the geometric sensitivity of radius to deflection increases with increasing radius (see Fig. 9). To illustrate this point, we have also added a value for the saggitus (calculated from measured focal length and clear aperture) to Tables 1 and 2.

Figure 7 shows the RMS slope error versus optical power for the 1-mm and 3.2-mm-thick substrates. One can see that the slope error for the 3.2-mm-thick substrate is roughly constant. On the other hand, the 1-mm-thick substrate shows a region of larger error of 0.03–0.1 diopters.

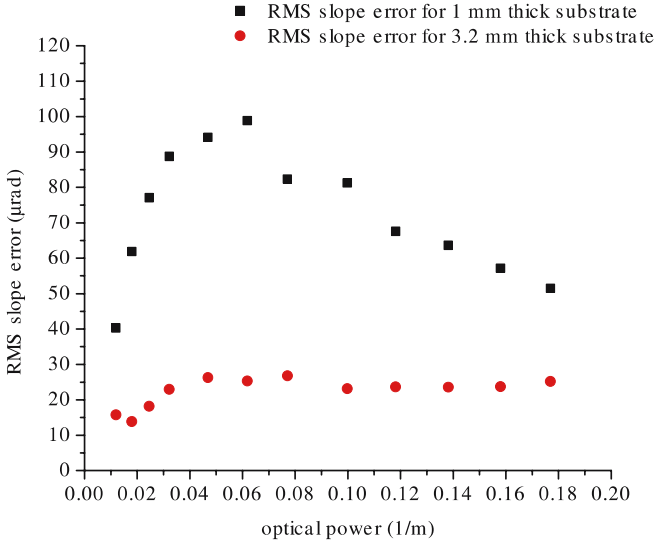

FIGURE 7 RMS slope error versus optical power for 1-mm and 3.2-mm-thick substrates

f (m)	Error (m)	RMS (µm)	RMS slope (µrad)	Saggitus (µm)
60.04	39.14	0.043	40.26	0.18
16.16	4.06	0.072	61.82	0.65
8.64	1.41	0.086	77.04	1.22
5.52	0.76	0.097	88.77	1.91
4.24	0.48	0.102	94.15	2.49
3.00	0.28	0.103	98.87	3.52
2.25	0.14	0.085	82.33	4.70
1.80	0.10	0.079	81.26	5.86
1.47	0.06	0.065	67.55	7.19
1.29	0.05	0.057	63.62	8.18
1.09	0.04	0.050	57.11	9.68
0.96	0.03	0.042	51.47	11.02
0.86	0.02	0.039	47.73	12.31
0.77	0.02	0.034	41.10	13.72
0.71	0.02	0.038	42.51	14.81
0.65	0.02	0.038	42.97	16.28
0.60	0.01	0.043	42.13	17.58
0.57	0.02	0.055	52.76	18.41

TABLE 1 Table of measured focal length for a 25.4-mm-diameter and 1-mm-thick mirror at a wavelength of 1054 nm. f = focal length; error = standard deviation of focal length measurement; RMS = RMS wavefront deviation of measured data from spherical fit; RMS slope = RMS slope error; saggitus = center deformation of optic

f (m)	Error (m)	RMS (µm)	RMS slope (µrad)	Saggitus (µm)
83.81	48.12	0.013	15.80	0.13
55.62	15.34	0.013	13.83	0.19
40.63	8.02	0.016	18.13	0.26
31.06	5.58	0.019	22.95	0.34
21.32	3.19	0.022	26.25	0.50
16.17	2.07	0.020	25.31	0.65
12.98	1.52	0.022	26.79	0.81
10.02	0.81	0.021	23.16	1.05
8.46	0.56	0.022	23.61	1.25
7.24	0.40	0.020	23.55	1.46
6.33	0.30	0.019	23.69	1.67
5.65	0.28	0.020	25.20	1.87

TABLE 2 Table of measured focal length for a 25.4-mm-diameter and 3.2-mm-thick mirror at a wavelength of 1054 nm. f = focal length; error = standard deviation of focal length measurement; RMS = RMS wavefront deviation of measured data from spherical fit; RMS slope = RMS slope error; saggitus = center deformation of optic

This may be due to an anisotropy in the pusher or retainer material. As the substrate deforms further, the reaction force becomes dominant and 'washes out' minor material anisotropies. If this is true, it would explain why the error varies far less in the case of the 3.2-mm-thick substrate since it requires a much higher force throughout its range.

Figure 8b shows the difference between the measured wavefront and the spherical fit. This saddle-like surface is typical for all the measurements we have taken and clearly points to an astigmatism. This effect might be due to machining errors in the parts or an anisotropy in the materials. These errors could be reduced by requiring tighter tolerances and by carefully choosing the appropriate annular pusher material. One should note that a wedge in the mirror substrates could have a large influence on the astigmatism. It is therefore advisable to use a mirror with minimum wedge if possible. In the current design, the RMS wavefront deviation for a 3.2-mm-thick mir-

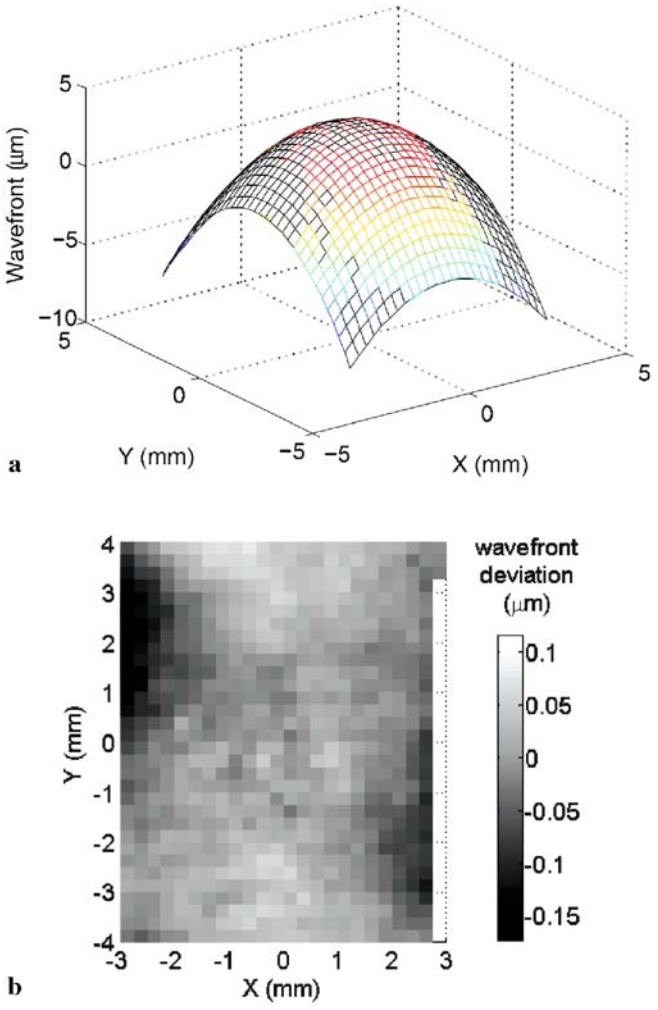

FIGURE 8 (**a**) Plot of measured wavefront data (*colored*) as well as the fitted sphere (*black*) for an $f = 77$ cm focal length mirror at 1-mm thickness and 25.4-mm diameter. (**b**) Contour error plot of the same measurement depicting the difference between measured data and fit

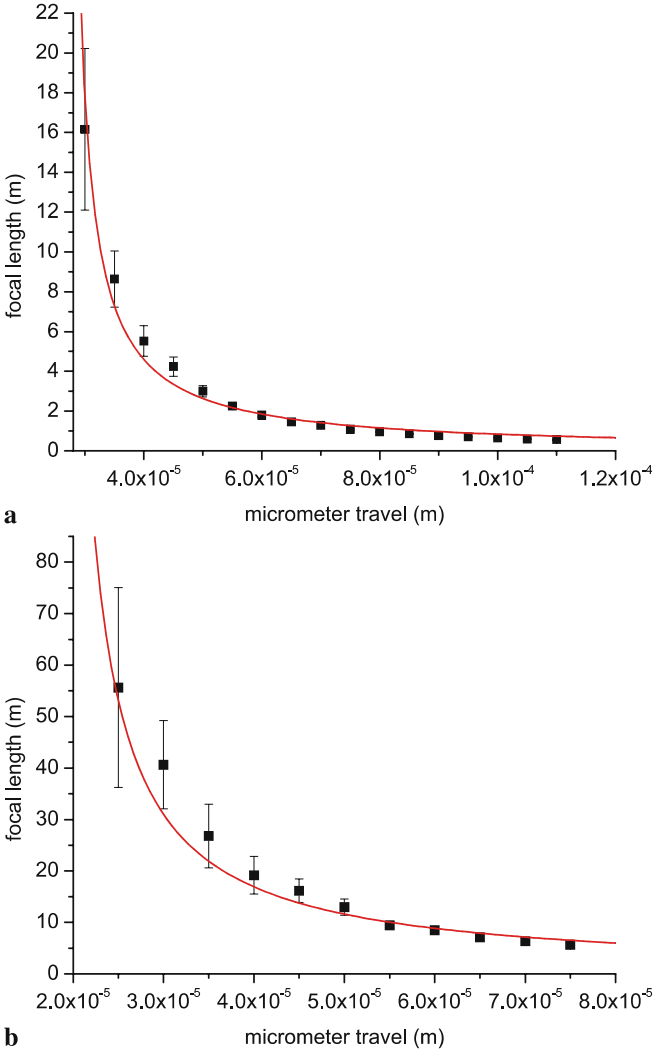

FIGURE 9 Plot of measured focal length versus micrometer travel for (**a**) 1 −mm-thick and (**b**) 3.2-mm-thick, 25.4-mm-diameter BK7 mirrors. The data was fitted to (5)

ror is $\leq \lambda/30$ and about $\leq \lambda/10$ for the 1-mm-thick mirror at $\lambda = 1054$ nm.

Figure 9 shows a plot of the measured focal length versus piston movement for 1-mm and 3.2-mm-thick mirrors. As expected, the focal length decreases (as the substrate curvature increases) with piston travel, as does the fitting uncertainty. It can be seen from Fig. 10 that the parabolic shape ($y = x^2/(4f)$) of the deformed mirror is defined by the contact line of the inner $N = 12.7$ mm and outer $M = 23.6$ mm diameters of the pusher and retainer ring. The piston travel P can then be expressed as $P = y(M/2) - y(N/2)$, yielding

$$P = \frac{M^2 - N^2}{16f} \iff f = \frac{M^2 - N^2}{16P} \implies$$
$$f_{\text{fit}} = \frac{M^2 - N^2}{16(P - P1)} \times P2\,, \qquad (5)$$

where $P1$ (μm) is a parameter related to the offset between the measured micrometer setting and the actual contact point of the micrometer tip with the substrate. The parameter $P2$ corresponds to the difference between the micrometer travel g and the actual piston travel P. This discrepancy is due to the overall flexure of the mirror housing. The values resulting from the fit are $P1 = 26.5\,\mu$m, $P2 = 2.5$ for the 1-mm-thick mirror, and $P1 = 18.0\,\mu$m, $P2 = 15$ for the 3.2-mm-thick mirror.

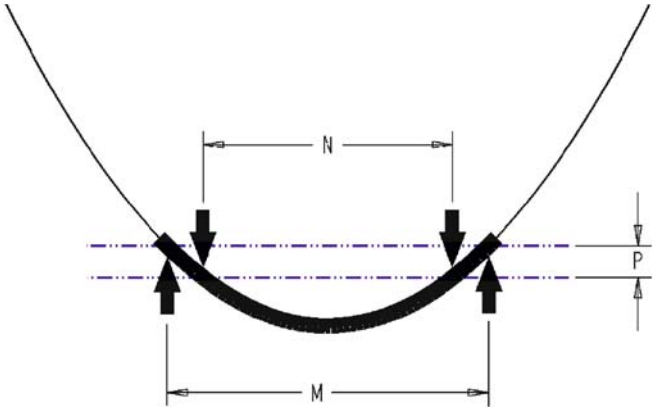

FIGURE 10 Conceptual schematic of bent mirror substrate after being deformed with an annular pusher of diameter N that is simply supported with an outer ring of diameter M. P is the travel distance of the pusher

4 Thermal lens compensation

After characterizing the performance of the deformable mirror with a Shack–Hartmann sensor, the deformable mirror assembly was placed in the rod amplifier section of our three-stage Optical Parametric Chirped Pulse Amplification (OPCPA) laser system. Figure 11 shows a partial conceptual overview of that system with the more detailed area of interest. The OPCPA seed beam is provided by a coherent Mira Ti:sapphire oscillator with 80-MHz repetition rate, 250-mW power, and 100-fs pulse width at 1054-nm wavelength. The OPCPA pump beam is provided by a seeded Nd:YAG ring regenerative amplifier operating at 10 Hz at an energy of 20 mJ in 2-ns pulse width. This s-polarized 1064-nm beam is injected into a 9-mm-diameter, flashlamp-pumped Positive Light Nd:YAG rod amplifier. The amplifier is pumped at a 10-Hz repetition rate with a flashlamp energy of 80 J per shot. After one pass through the amplifier and Faraday rotator, the beam encounters a quarter-wave plate and an end mirror (in this case our deformable mirror), which together rotate the polarization by 90° to p-polarization and reflect the beam towards a second pass through the rod amplifier. After ejection at the polarizing beam splitter (PBS), the amplifier output is frequency doubled, demagnified, and relay imaged to provide the pump at the crystal in an optical parametric am-

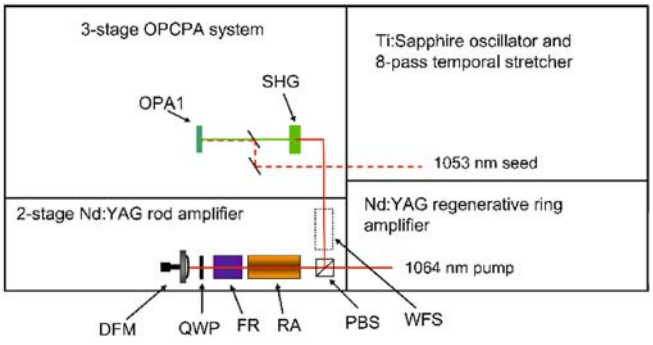

FIGURE 11 Partial conceptual overview of the laser system. An s-polarized 20-mJ, 2-ns, 532-nm beam exits the regenerative ring amplifier and is transmitted by a polarizing beam splitter (PBS). After amplification in the 9 × 100 mm diameter Positive Light rod amplifier (RA) and transmission through the Faraday rotator (FR) and the quarter-wave plate (QWP), the beam is reflected off the deformable mirror (DFM). The p-polarized amplified beam is reflected off the PBS and frequency doubled by type-II second-harmonic generation (SHG) in a 30-mm-thick Potassium Dideuterium Phosphate (DKDP) crystal. This beam is then relay imaged onto the OPA crystal. Wavefront measurements were performed with a movable Shack–Hartmann wavefront sensor (WFS)

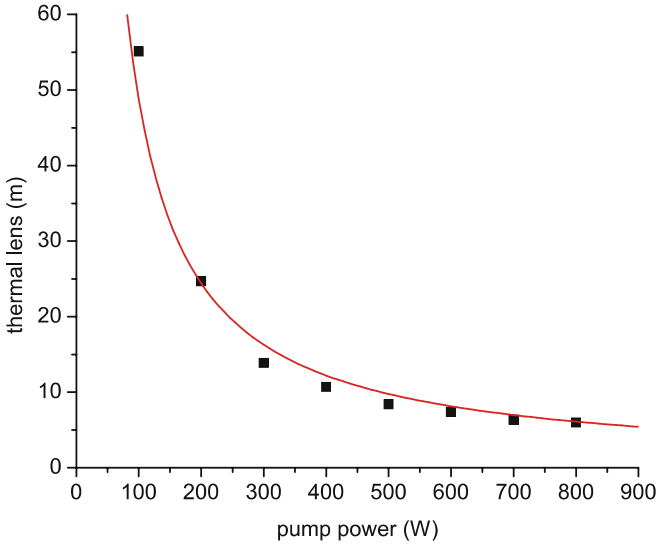

FIGURE 12 Plot of the single-pass thermal lens versus pump power in the rod amplifier. Theoretical curve (not a fit) for a single-pass thermal lens (7) for a heat conversion of 5% from pump power to thermal load

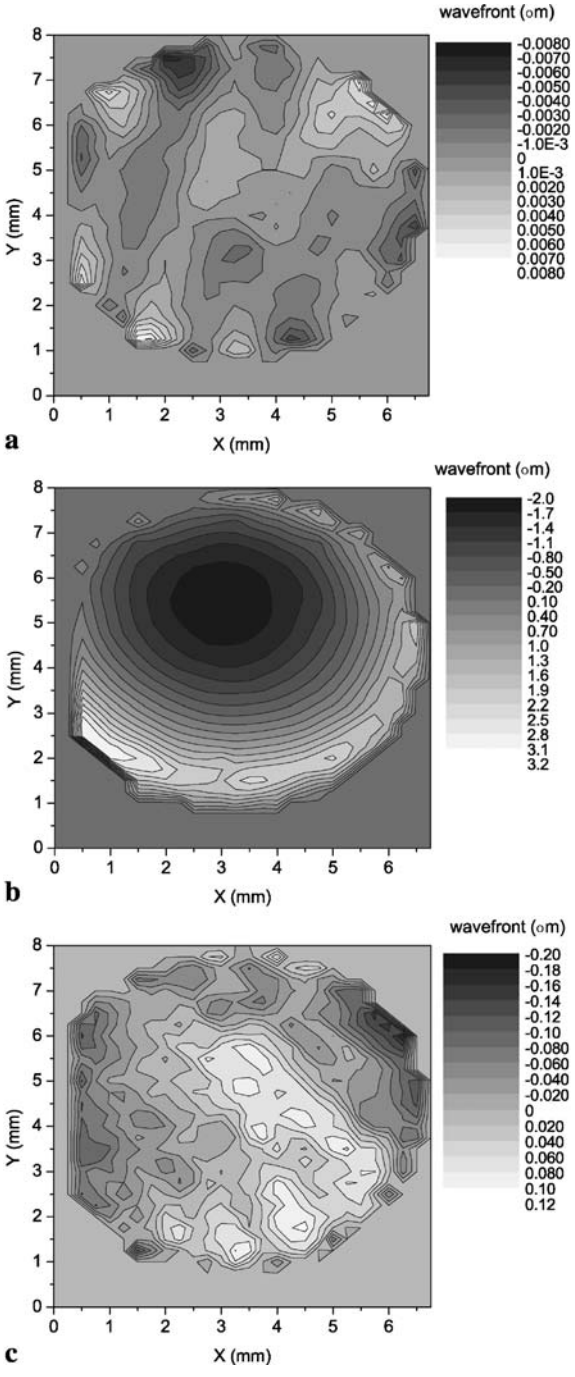

FIGURE 13 (**a**) Baseline measurement of wavefront at zero pump power. (**b**) Thermally induced wavefront at a pump power of 800 W. Note: the wavefront center is slightly shifted off-center due to an artifact in the wavefront-sensing software. (**c**) Corrected wavefront using the convex deformable mirror

plifier (OPA). Thermal lensing of the amplified pump pulse was measured by placing a Shack–Hartmann wavefront sensor in the beam line of the 1064-nm pump beam that is ejected after amplification (see Fig. 11). The measured wavefront was fitted to a sphere in order to yield an effective focal length that results from a double pass through the rod amplifier medium. Knowing the distance $l = 30.5$ cm between the rod center and the retro-reflecting deformable mirror, one can extract the single-pass thermal lens using the following equation [9]:

$$\frac{1}{f} = \frac{1}{f_1} + \frac{1}{f_2} - \frac{2 \times l}{f_1 f_2}\,, \tag{6}$$

where f is the measured focal length and $f_1 = f_2$ is the single-pass thermal lens. Figure 12 shows the single-pass thermal lens versus pump power. The data was compared to a theoretically derived thermal lens f_T, assuming homogeneous pumping along a cylindrical surface with strictly radial heat flow [1]:

$$f_T = \frac{1}{2}\frac{KA}{P_H}\frac{dn}{dT}\,, \tag{7}$$

where $K = 14\,\mathrm{W/(m\,K)}$ is the thermal conductivity of Nd:YAG [1], A is the cross-sectional area of the amplifier rod, $P_H = 0.05 P_{total}$ is the effective heat deposited in the Nd:YAG rod, and $dn/dT = 7.3 \times 10^{-6}\,1/\mathrm{K}$ is the differential change of refractive index with temperature [1]. One can see from Fig. 12 that there is good agreement between the theoretically predicted focal length and the experiment assuming a commonly used heat conversion of 5%.

Thermal lensing was compensated by monitoring the wavefront while slowly turning the micrometer at the end of the deformable mirror (DFM) assembly. The piston was moved in increments of about 10 μm to a total travel of 75 μm. Figure 13a shows a baseline wavefront measurement with the deformable mirror being in the undeformed state and the rod amplifier being shut off. The wavefront software was calibrated to the relaxed mirror itself. In that case, the peak to valley ($P - V$) wavefront error was only $P - V = 0.014$ μm, which defines a lower limit for the error in the measurement. When the pump power was increased, spherical wavefront deformation was observed. Figure 13b shows the wavefront at an operating pump power of 800 W. The wavefront deformation grew to $P - V = 5.02$ μm, but could be compensated by the deformable mirror ($P - V = 0.29$ μm) as seen in Fig. 13c.

The wavefront sensor was subsequently removed and the frequency-doubled pump beam profiles at the OPA relay plane were measured. Figure 14 shows the beam profiles and their central lineouts for compensated and uncompensated thermal lenses at the plane of the OPA crystal. It can clearly be seen that the average intensity in the beam is raised and that the peak to average modulation has been reduced. In addition, the FWHM has increased from 380 μm to about 650 μm. This allows for a more uniform pumping of the OPA crystal, leading to improved conversion efficiency in the OPA process and better beam quality.

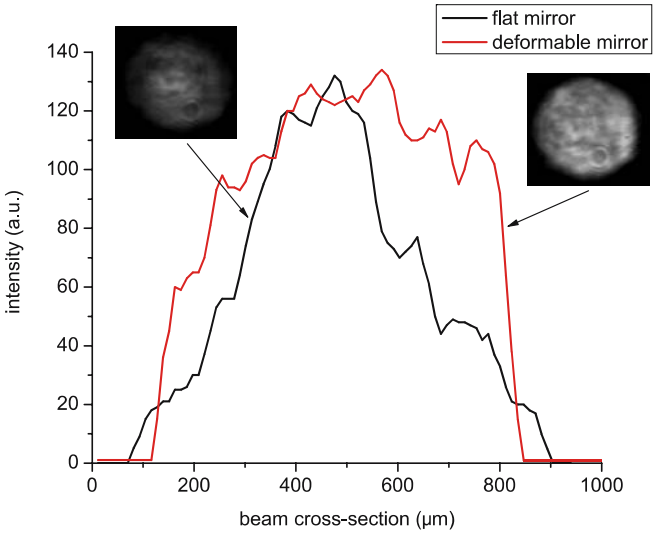

FIGURE 14 Lineouts of the pump beam profile at the OPA crystal plane

5 Conclusion

We have presented a new design for a deformable mirror holder [10] that creates a large-area convex parabola with optical surface quality. The design has been modeled in detail and its performance has been tested in quantitative wavefront measurements. This assembly can easily be expanded to larger diameters leading to a wide variety of applications.

ACKNOWLEDGEMENTS Sandia is a multiprogram laboratory operated by Sandia Corporation, a Lockheed Martin Company, for the United States Department of Energy's National Nuclear Security Administration under Contract No. DE-AC04-94AL85000.

REFERENCES

1 W. Koechner, B. Bass, *Solid-State Lasers* (Springer, New York, 2003)
2 P.H. Sarkies, Opt. Commun. **31**, 189 (1979)
3 T. Graf, E. Wyss, M. Roth, H.P. Weber, Opt. Commun. **190**, 327 (2001)
4 E. Wyss, M. Roth, T. Graf, H.P. Weber, IEEE J. Quantum Electron. **QE-38**, 1620 (2002)
5 G.V. Vdovin, S.A. Chetkin, Kvant. Elektron. Moskva, **20**(2), 167 (1993); translated in IEEE J. Quantum Electron. **QE-23**(2), 141 (1993)
6 U.J. Greiner, H.H. Klingenberg, Opt. Lett. **19**, 1207 (1994)
7 Y.C. Warren, B.G. Richard, *Roark's Formulas for Stress and Strain*, 7th edn. (McGraw-Hill, New York, 2002)
8 Schott, Optical glass catalog (1996) [http://www.us.schott.com/sgt/english/download/n-bk7.pdf]
9 M. Born, E. Wolf, *Principles of Optics*, 7th edn. (Cambridge University Press, Cambridge, UK, 1999)
10 D. Headley, M. Ramsey, J. Schwarz, U.S. Patent Application No. 11/017337, filed on 20 December 2004